Impact of mismatched and misaligned laser light sheet profiles on PIV performance

K. Grayson[1] · C. M. de Silva[1] · N. Hutchins[1] · I. Marusic[1]

Abstract

The effect of mismatched or misaligned laser light sheet profiles on the quality of particle image velocimetry (PIV) results is considered in this study. Light sheet profiles with differing widths, shapes, or alignment can reduce the correlation between PIV images and increase experimental errors. Systematic PIV simulations isolate these behaviours to assess the sensitivity and implications of light sheet mismatch on measurements. The simulations in this work use flow fields from a turbulent boundary layer; however, the behaviours and impacts of laser profile mismatch are highly relevant to any fluid flow or PIV application. Experimental measurements from a turbulent boundary layer facility are incorporated, as well as additional simulations matched to experimental image characteristics, to validate the synthetic image analysis. Experimental laser profiles are captured using a modular laser profiling camera, designed to quantify the distribution of laser light sheet intensities and inform any corrective adjustments to an experimental configuration. Results suggest that an offset of just 1.35 standard deviations in the Gaussian light sheet intensity distributions can cause a 40% reduction in the average correlation coefficient and a 45% increase in spurious vectors. Errors in measured flow statistics are also amplified when two successive laser profiles are no longer well matched in alignment or intensity distribution. Consequently, an awareness of how laser light sheet overlap influences PIV results can guide faster setup of an experiment, as well as achieve superior experimental measurements.

1 Introduction

The intensity distribution and alignment characteristics of a laser beam can vary over time, due to factors such as ageing system components and the drifting alignment of laser optics. These variations can have a particular impact on laser-based flow visualisation measurements, which rely on stable and uniform laser beam intensity distributions. Measurement techniques which use dual-cavity lasers, such as particle image velocimetry (PIV), are especially vulnerable to these changes, since the characteristics of each laser cavity can drift independently. Mismatch in the behaviour of the two laser cavities can degrade the correlation of resulting PIV image pairs, and subsequently impact measured flow quantities. Therefore, quantifying and refining laser overlap and profile distributions can help to improve experimental results, and can be crucial when performing more challenging PIV measurements involving multiple pulses (e.g., 3 or 4 pulse PIV) or large fields of view.

Two misaligned, but otherwise identical light sheets in a PIV experiment have an effect equivalent to an out-of-plane velocity component in the flow (see Fig. 1), increasing the out-of-plane loss of particle pairs under typical flow conditions (Adrian and Westerweel 2011; Scharnowski and Kähler 2016; Scharnowski et al. 2017). Under extreme out-of-plane velocity conditions, this behaviour may even be exploited to minimise out-of-plane loss-of-pairs by deliberately misaligning laser sheets (Kähler and Kompenhans 2000). A number of studies have investigated the effects of out-of-plane loss-of-pairs on PIV results and the impact on PIV uncertainties (Nobach and Bodenschatz 2009; Nobach 2011; Scharnowski and Kähler 2016; Scharnowski et al. 2017). However, while out-of-plane velocity components may be unavoidable in a given flow of interest, laser light sheet mismatch can be identified and corrected prior to performing an experiment. This correction of the experimental setup prior to capturing PIV images decreases the error associated with the measurement, yielding higher quality results.

Despite the importance of laser light sheet overlap and the similarity of laser profiles for high-quality PIV

✉ K. Grayson
kristiangrayson@gmail.com

[1] Department of Mechanical Engineering, University of Melbourne, Parkville, VIC 3010, Australia

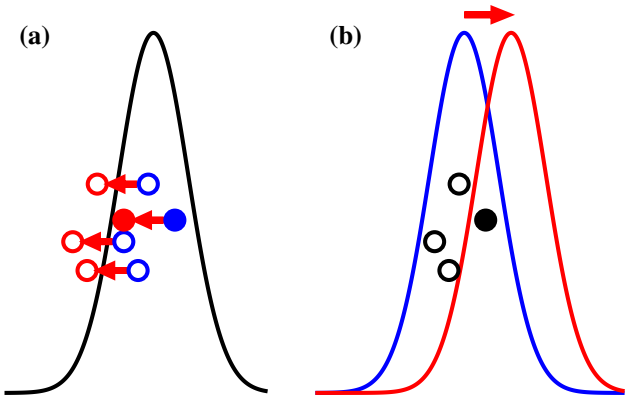

Fig. 1 Sketch of laser light sheet intensity distributions, illustrating the equivalence of **a** out-of-plane velocities and **b** out-of-plane misalignment of the laser sheet on the resulting illumination of tracer particles. Blue and red outlines indicate positions under laser pulses 1 and 2, respectively, while black outlines represent unchanged positions over pulses 1 and 2. Solid circles show particles with similar pulse 1 and 2 illumination, while hollow circles represent particles with unequal illumination, such that they have little or no contribution to correlation

measurements, careful refinement of laser shape and alignment is sometimes overlooked during the setup of experiments. Experimental papers often neglect any mention of light sheet parameters and behaviour (the quality of light sheet overlap, for example, which may offer some context to the results), while others may mention a light sheet thickness without any explanation of the measurement method or width criteria used to define what is often assumed to be a Gaussian profile. We note that laser sheet thicknesses can be extracted from stereo PIV measurements (Wieneke 2005), and tomographic PIV allows an approximation of the laser sheet intensity distribution to be reconstructed (Blinde et al. 2015). In practice, indications of experimental laser overlap quality can also be obtained by capturing two PIV images with a very small time interval (for near-zero particle displacement) and examining the correlation magnitude, or by calculating the correlation/autocorrelation volume ratio from any PIV image pair (Scharnowski and Kähler 2016; Scharnowski et al. 2017). However, both these techniques do not inform the changes which may be necessary to improve the laser overlap performance during laser alignment, nor detail the nature of each light sheet's intensity distribution. Therefore, from these methods, an experimentalist can learn if they have a light sheet mismatch problem, but they do not know the necessary course of corrective action. A more rigorous approach is required for more detailed measurements of the laser sheet in stereo and tomographic PIV configurations, as well as quantifying any of the laser parameters found in 2D PIV setups.

Some studies do control and specify the laser thickness by employing a fixed-width slit, which can approximate a top hat light sheet profile. Assuming negligible laser beam divergence, the laser sheet thickness is, therefore, equal to the slit width (Scarano et al. 2006; Elsinga et al. 2006; Blinde et al. 2015). This method, however, does not account for variations in laser intensity distribution or overlap. Laser burn tests can be a useful method of comparing light sheet thickness and estimating sheet separations, as was used in a dual-plane PIV study by Ganapathisubramani et al. (2005). However, burn papers generally offer insufficient resolution and dynamic range to analyse the sheet intensity distribution in detail. Imaging a surface illuminated by a laser sheet can yield further information regarding the intensity distribution. Fond et al. (2015) imaged samples of laser sheets using a piece of paper normal to the laser beam, while Kähler and Kompenhans (2000) and Mistry and Dawson (2014) imaged the sheet on a white plate, inclined relative to the laser sheet for increased resolution. Electronic laser profiling methods are increasingly being used to quantify laser intensity distributions and alignment with greater sensitivity and repeatability. Studies have used a knife edge laser profiler (Mullin and Dahm 2005), laser profiles of the laser beam prior to manipulation by the sheet optics (Brücker et al. 2012), and camera-based laser profilers for monitoring laser sheet distributions and alignment (Mullin and Dahm 2005; Pfadler et al. 2009; Naka et al. 2016). Camera-based laser profilers tend to offer the greatest flexibility with typical pulsed PIV lasers, since they are able to easily capture dynamic (shot-to-shot), as well as static, laser beam behaviours.

Commercial camera-based laser profiling devices, such as that used by Naka et al. (2016), are available to measure laser beam distributions and alignments, but are often expensive and can lock users into closed, proprietary software packages and image formats. They also may not be totally 'ready-to-run', since it is likely that additional optics will be required to attenuate the high power laser beams used routinely in PIV measurements. At the opposite end of the cost spectrum, however, researchers are using modified webcams for beam alignment and profiling with great success (Cignoli et al. 2004; Andrèbe et al. 2011; Langer et al. 2013). Webcams offer an extremely low cost, off-the-shelf means of measuring laser beam profiles, requiring only the removal of their camera lens and the addition of attenuating optics to operate. This configuration has been demonstrated in applications from laser- induced fluorescence measurements to lasers used in fusion reactors (Cignoli et al. 2004; Andrèbe et al. 2011), the only limitation being the relatively small sensor size which may not entirely capture unfocused PIV laser beams.

This study examines the impact of laser sheet misalignment and profile mismatch in PIV experiments by first isolating these parameters in simulations of particle images, and estimating the sensitivity of laser configurations on PIV measurement quality and flow statistics. A modular, low-cost

laser profiling device is then used to measure and compare experimental laser misalignments to the simulated and predicted behaviours in a PIV measurement.

Throughout this paper, the coordinate system x, y, and z refers to the streamwise, spanwise, and wall-normal directions, respectively. Corresponding instantaneous streamwise, spanwise, and wall-normal velocities are denoted by u, v, and w. Overbars indicate averaged quantities, and a superscript + refers to normalisation by inner scales, for example, $u^+ = u/U_\tau$ and $x^+ = xU_\tau/\nu$, where U_τ is the friction velocity and ν is the kinematic viscosity of the fluid.

2 Simulating laser sheet mismatch

The effects of laser sheet mismatch can be systematically investigated with the use of simulated PIV images. This enables control over all measurement parameters, while still considering experimentally realistic flows. Consequently, the variables of interest can be isolated and their impacts examined in detail.

2.1 Simulation methodology

The simulations performed in this study use an in-house PIV simulation and processing Matlab code, originally developed for Tomographic PIV simulations (see de Silva et al. 2012). This program has since been modified for 2D planar PIV simulations with increased functionality, enabling greater scope to generate more realistic PIV images. These improvements include more rigorous modelling of PIV image noise behaviours, particle shape and size variations, imperfect camera focus, and loss of sharpness at the edges of a synthetic image. Crucially, the light sheet profile can also be defined, allowing the implementation of Gaussian, top hat and super-Gaussian cross sections, in addition to applying custom profiles using data from a laser profiling camera. The width and alignment of each laser pulse can also be specified, a feature which enables the mismatch analysis presented in this study.

Following prior work (de Silva et al. 2012; Worth et al. 2010), the simulation procedure uses DNS velocity fields to displace randomly located virtual particles and generate synthetic PIV particle images. These images are subsequently fed into a PIV processing and correlation code, which applies a 'template matching' normalised cross-correlation scheme based on the work of Lewis (1995) (details regarding the implementation of this scheme can be found in de Silva et al. 2012). The resulting velocity fields can be directly compared to the input DNS velocity fields and errors can be calculated. Using this method, the degree of laser light sheet overlap can be systematically varied and comparisons between the resulting synthetic PIV velocity fields can be made.

2.2 Simulation parameters

For the present study, the turbulent boundary layer DNS data set from Sillero et al. (2013) at $Re_\theta = 6500$ is used. Synthetic two-pulse particle images are generated over a streamwise–spanwise plane using the parameters summarised in Table 1, with simulations repeated for Gaussian, super-Gaussian, and top hat light sheet profiles. Infinite depth of field and no image noise is modelled in this simulation, while experimentally representative particle densities, sizes, and size variations are used. A multipass correlation algorithm with window deformation is applied to process the resulting synthetic images from a 64×64 pixel interrogation window down to a final interrogation window size of 32×32 pixels, or approximately 20×20 viscous units. Results are averaged over ten distinct DNS flow fields, as well as over cases that interchangeably misalign pulse 1 (with pulse 2 fixed), and misalign pulse 2 (with pulse 1 fixed), to avoid biasing effects.

The Gaussian and super-Gaussian light intensity profiles, $I_0(z)$, across the light sheet-normal direction z, are modelled by Eq. 1, using $N = 2$ and $N = 10$, respectively. In this expression, $I_{\max}$ describes the maximum intensity of the profile, while z_0 refers to the midpoint of the light sheet distribution and σ denotes the profile's standard deviation. The width of the simulated top hat light sheet profile is matched to the Gaussian profile standard deviation, σ, and the resulting three profiles are illustrated in Fig. 2.

$$I_0(z) = I_{\max} \times \exp\left[-\frac{1}{2}\left(\frac{z - z_0}{\sigma}\right)^N\right] \quad (1)$$

Two separate laser mismatch scenarios are considered. In case 1, two identical light sheet profiles are systematically translated relative to one another, as shown schematically using Gaussian profiles in Fig. 3a. This scenario is directly equivalent to the presence of an out-of-plane flow velocity component. The light sheet thickness used in this simulation

Table 1 Summary of simulation parameters

Parameter	Value
Measurement plane	Streamwise × spanwise
Re_θ	6500
DNS domain ($x^+ \times y^+$)	4200×6300
Wall-normal height (z^+)	240
Image resolution	1.6 viscous units/pixel
Image bit-depth	16 bit

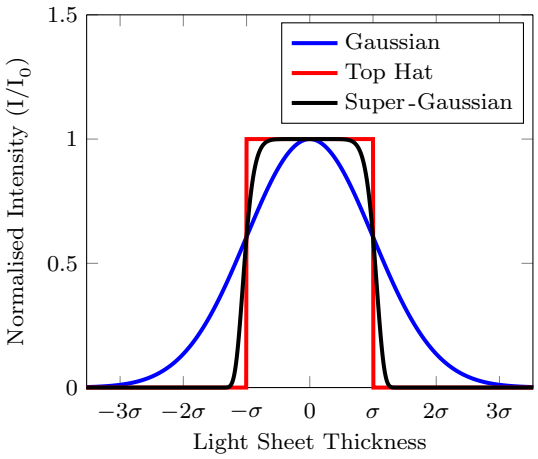

Fig. 2 Cross section of simulated laser sheet profiles

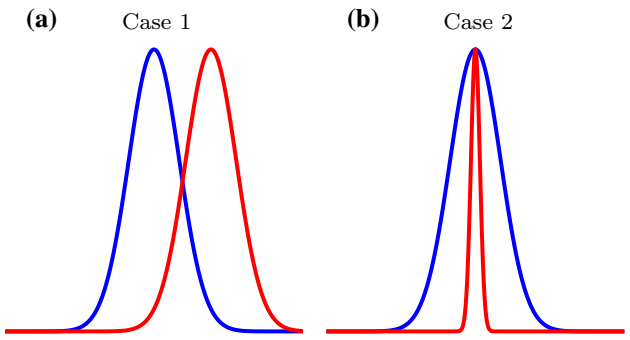

Fig. 3 Sample **a** case 1 shift misalignment and **b** case 2 width mismatch, applied to Gaussian light sheet profiles. The blue curve illustrates the intensity profile of laser pulse 1, while the red curve represents the intensity profile of laser pulse 2

case remains fixed, with a standard deviation of 7.1 viscous units. This thickness was determined by performing a Gaussian fit onto a representative experimental light sheet profile. Light sheet misalignment is simulated in scenarios ranging from perfect overlap to a shift equivalent to a 3σ light sheet offset.

Case 2 investigates the impact of different light sheet widths on PIV performance, as shown in Fig. 3b. In this scenario, both laser pulses remain centred about a fixed location, but the standard deviation of one light sheet profile (from one laser pulse) is varied, while the other light sheet profile (from the other laser pulse) remains fixed. Scenarios have been simulated with laser profile standard deviations ranging from 0.4 viscous units to 7.1 viscous units, while the fixed light sheet profile uses a constant standard deviation of 7.1 viscous units. Therefore, the mismatched case always has a narrower laser sheet profile than the reference 7.1 viscous unit standard deviation case.

2.3 Quantification of laser mismatch

To compare the results of cases 1 and 2 on a common set of axes, a metric is needed to quantify the mismatch of successive laser pulses. Early work on out-of-plane loss-of-pairs by Keane and Adrian (1992) established a parameter, F_O, which is defined by Eq. 2, assessing the proportion of particles between the first and second PIV images which can be paired. I_{01} and I_{02} represent the light sheet intensity profiles of laser pulses 1 and 2, respectively, while z_{01} and z_{02} indicate their sheet centre locations and Δz denotes the out-of-plane particle displacement (considered to be zero in this analysis due to averaging to isolate mismatch effects). $F_O = 1$ corresponds to when every particle found in two successive PIV images can be paired together, while $F_O = 0$ indicates that no particles can be paired from the image set. Intermediate values reflect partial pairing of particles.

$$F_O = \frac{\int I_{01}(z - z_{01}) \cdot I_{02}(z - z_{02} - \Delta z)\,\mathrm{d}z}{\int I_{01}(z) \cdot I_{02}(z)\,\mathrm{d}z} \tag{2}$$

The F_O parameter offers a good measure of singular out-of-plane velocity and light sheet-normal laser misalignment effects, which serves its original, intended purpose. However, this parameter does not capture other scenarios, such as when laser sheet profiles have differing widths, as applied in case 2 of this study. Therefore, a modified form of F_O, first proposed and assessed in Scharnowski et al. (2017), is used in this paper[1] and shown in Eq. 3. This adjustment to the F_O expression has no impact on the calculation of out-of-plane velocity effects for identical light sheet profiles, while enabling laser profile width and shape mismatches to also be distinguished.

$$F_O = \frac{\int I_{01}(z - z_{01}) \cdot I_{02}(z - z_{02} - \Delta z)\,\mathrm{d}z}{\sqrt{\int I_{01}^2(z)\,\mathrm{d}z \cdot \int I_{02}^2(z)\,\mathrm{d}z}} \tag{3}$$

2.4 Quality of correlation

Using the revised expression for F_O to generalise the mismatch conditions applied in these simulations, the impact on correlation quality can be assessed under different laser alignment scenarios. Figure 4a shows the average correlation coefficient ($\bar{R}_C$) from both simulation cases 1 and 2, which is calculated by averaging together the correlation coefficients

[1] The final form of the modified F_O expression shown here was developed in collaboration with Sven Scharnowski and Christian Kähler from Bundeswehr University, Munich, after the initial submission of this article. It is comprehensively outlined in Scharnowski et al. (2017).

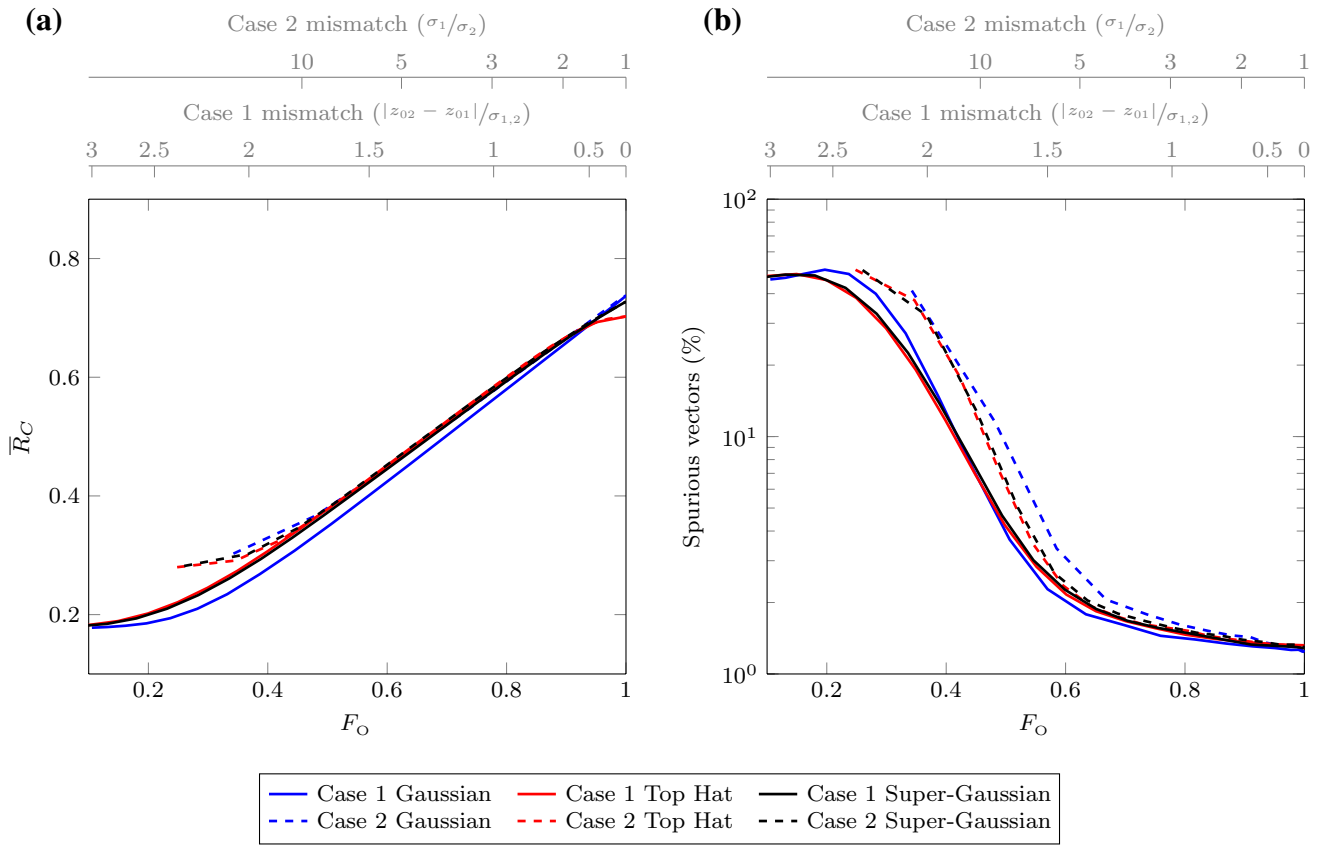

Fig. 4 Simulation results illustrating the impact of laser profile mismatches on **a** average correlation coefficient and **b** the proportion of spurious vectors. Case 1 shift mismatch results are shown using solid lines, while case 2 width mismatch results are shown with dashed lines. Additional scales above each plot, shown in grey, correspond to the magnitude of case 1 light sheet offset, normalised by the standard deviation, and the case 2 light sheet width ratio for Gaussian light sheet profiles

from each final interrogation window of the raw velocity fields. The scales above each plot in Fig. 4 show the case 1 and 2 Gaussian profile mismatch required for a range of F_O values. Case 1 mismatch is indicated by the magnitude of the light sheet offset, normalised by the standard deviation of the light sheet profile (case 1 considers identical light sheet widths). Case 2 mismatch is shown by the ratio between the standard deviations of the thick and thin light sheets. We note that the maximum average correlation remains below 0.8 due to the turbulent DNS flow field used in this simulation, in addition to other sources of error from PIV processing. The three tested laser profile shapes exhibit similar behaviour in Fig. 4a, showing steady, near-linear degradation of mean correlation coefficient for both shift and width mismatch simulations (cases 1 and 2, respectively), until excessive mismatch flattens the mean correlation at the correlation noise floor. Case 2 simulations produce a higher noise floor than found with case 1, due to reduced particle image densities from the narrowing of one light sheet. The revised F_O expression is able to distil consistent behaviour from shift and width misalignments, despite complex interactions under these scenarios influencing the particle image pairs, interrogation window particle image densities, and variations in particle image intensities.

Outlier detection can be performed on the simulation results from both cases 1 and 2, like any typical PIV experiment data, to check for and remove spurious vectors. To this end, the normalised median test of Westerweel and Scarano (2005) is applied to these results, using the same recommended parameters for all scenarios. The resulting percentage of spurious vectors detected from the velocity vector fields in different laser sheet shift and width mismatch simulations are plotted on linear-log axes, as shown in Fig. 4b. The results show that both case 1 and 2 simulations with moderately high F_O values ($F_O > 0.65$) contain few spurious vectors, consistent with their reasonably well aligned and matched laser profiles. However, the proportion of spurious vectors detected by the normalised median test increases rapidly for values of F_O less than 0.65. This $F_O \sim 0.65$ threshold is universally observed under both shift (case 1) and width (case 2) mismatch scenarios for all tested light sheet profile shapes.

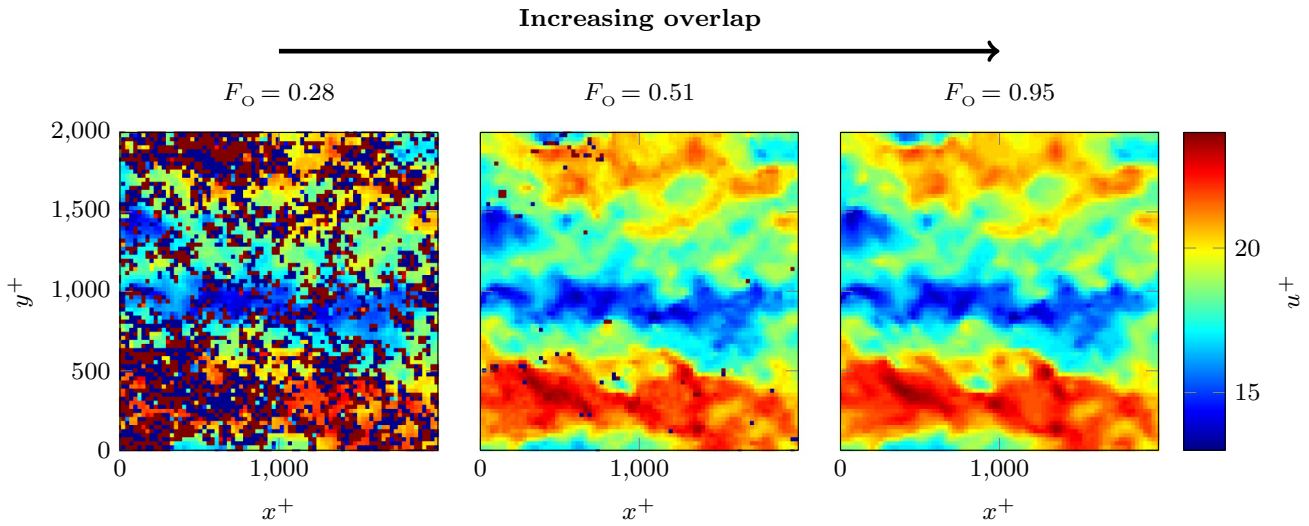

Fig. 5 Comparison of raw instantaneous streamwise velocity fields from case 1 simulations with a Gaussian light sheet profile. Streamwise and spanwise dimensions are denoted by x and y, respectively

It corresponds to simulations with shift offsets ranging from $1.35\,\sigma$ for a Gaussian sheet profile, up to $2.4\,\sigma$ for a super-Gaussian profile, or when the width of one laser sheet is between 2.4 (for a top hat profile), and 4.3 (for a Gaussian profile) times greater than the other. A light sheet width mismatch, where one light sheet is more than twice as wide as the other may be readily identified using a variety of laser measurement techniques, and may even be observed with a quick visual check of the laser. However, a $1.35\,\sigma$ shift offset of two laser profiles is more subtle and detection is likely to require more rigorous laser profiling. This reinforces the zero-displacement synthetic image results presented in Scharnowski et al. (2017), and highlights that F_O and measurement quality are more sensitive to out-of-plane laser alignment than to mismatches in light sheet width.

For experiments with a laser sheet thickness on the order of 1 mm, an offset of only 0.35 mm is sufficient to degrade F_O to 0.65 (assuming a top hat profile). A laser sheet misalignment of this order under experimental conditions may be difficult to identify and correct using visual alignment methods, burn tests or other techniques unable to capture the light sheet's intensity distribution in detail. Furthermore, very small changes in laser sheet mismatch around the spurious vector threshold for each case, either from changes to the laser's optical configuration or from subtle shot-to-shot laser instability (see Grayson et al. 2017), can have large consequences for the proliferation of spurious vectors. For example, changing F_O from 0.5 to 0.4 can increase the proportion of detected spurious vectors from 3.7 to 14.8%, and only involves an increase in the pulse shift from 1.65 to 1.95 σ (or an additional misalignment of 0.05 mm for a 1 mm-thick laser sheet). A misalignment of this magnitude could, therefore, be the difference between noisy, but acceptable PIV measurements, and effectively unusable data sets.

To further illustrate the impact of laser misalignment, Fig. 5 presents raw instantaneous streamwise velocity fields. Case 1 simulations using a Gaussian light sheet profile are compared with F_O values of $F_O = 0.95$ (near 'ideal', or a shift of $0.45\,\sigma$), $F_O = 0.51$ (just past the spurious vector threshold) and $F_O = 0.28$ (well beyond the spurious vector threshold). While the $F_O = 0.95$ velocity field appears visually smooth, a scattering of clear outliers becomes visible

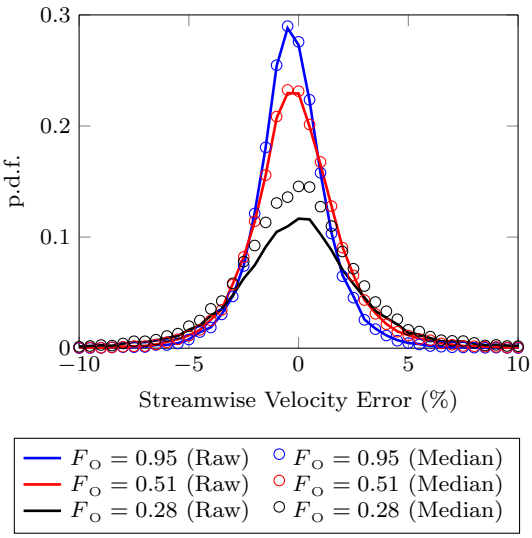

Fig. 6 Comparison of the streamwise velocity error probability density function from the case 1 Gaussian instantaneous velocity fields shown in Fig. 5. The raw velocity fields generate error distributions shown by the solid lines, while velocity errors after the application of the normalised median test are shown by the open circles

once $F_O = 0.51$. Closer analysis of these raw instantaneous fields using the probability density function of the streamwise velocity error (shown in Fig. 6) also reveals the presence of additional noise in the $F_O = 0.51$ velocity field that is not detected by the normalised median test (the error p.d.f. of each velocity field after the application of the median test is shown by the open circles). This noise increases the observed streamwise velocity error, broadening the error distribution and consequently lowering the p.d.f. peak. Therefore, even if the clearly spurious vectors are removed from this field, fine scale noise due to poor laser overlap continues to degrade a measurement's accuracy. At the point F_O reaches 0.28, the velocity field is practically unusable due to the high density of spurious vectors.

2.5 Errors in flow statistics

It is worth noting that even though we do not see a sharp increase in the number of spurious vectors until $F_O < 0.65$, the sensitivity of a measurement's laser misalignment can depend on the flow statistics of interest. Figure 7 shows the percentage error associated with streamwise mean velocity and turbulence intensity statistics, after spurious vectors have been removed via the normalised median test. Case 1 and 2 simulations and all tested light sheet profile shapes exhibit consistent error behaviour.

Predictably, the mean velocity measurement has a lower baseline error at $F_O = 1$ compared with turbulence intensity, which is a higher order statistical measure. What is more revealing, however, is a comparison of the breakpoints in these statistics, after which the error grows more rapidly. The turbulence intensity jumps to higher errors at a greater F_O value (around $F_O \sim 0.6$) than observed in the mean velocity (approximately $F_O \sim 0.5$).

To further investigate these trends, the error results from each simulation case were averaged together for improved convergence, due to their relatively consistent behaviour. The resulting error averages for the streamwise mean, variance (turbulence intensity), skewness and kurtosis statistics are shown in Fig. 8a on linear axes, normalised by their error under 'ideal' overlap conditions ($F_O = 1$). The error breakpoints exhibit a clear trend towards higher F_O values when considering higher order flow statistics. To quantify this trend, the F_O corresponding to a given increase in a statistic's error (e.g., a doubling in error, or a ×2 factor) was recorded. This process is equivalent to the intersection between the normalised error of the flow statistic and a horizontal line at the desired maximum error criterion (shown in Fig. 8a at 2% normalised error for a ×2 error criterion). Three maximum error criteria were considered for comparison (×1.5, ×2, and ×3 factors), and the corresponding F_O thresholds for each flow statistic are shown in Fig. 8b. Results suggest that the lowest F_O achievable under these criteria can range from $F_O = 0.5$ for mean velocities, up to $F_O = 0.7$ for kurtosis. This defines a lower limit for F_O, but higher F_O values are clearly desirable for greater margin in laser and error performance. It is, therefore, evident that the measurement quality and quantities of interest can determine the importance of maintaining good matching of

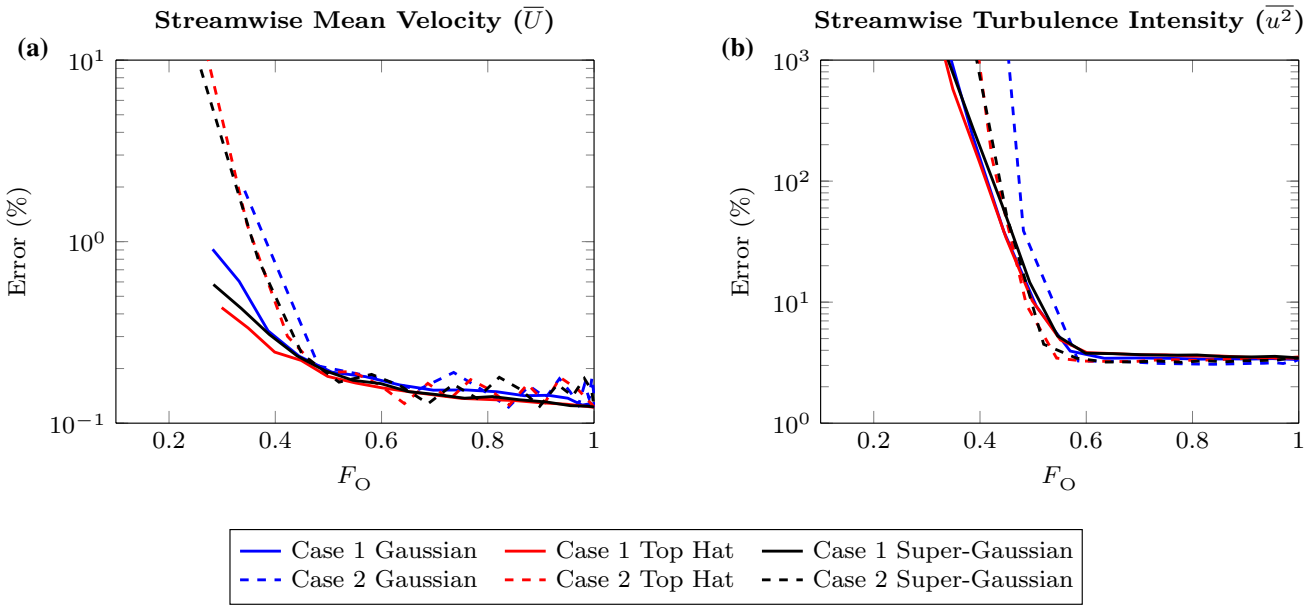

Fig. 7 Errors associated with **a** streamwise mean velocity ($\overline{U}$) and **b** turbulence intensity ($\overline{u^2}$). Case 1 shift mismatch results are shown using solid lines, while case 2 width mismatch results are shown with dashed lines

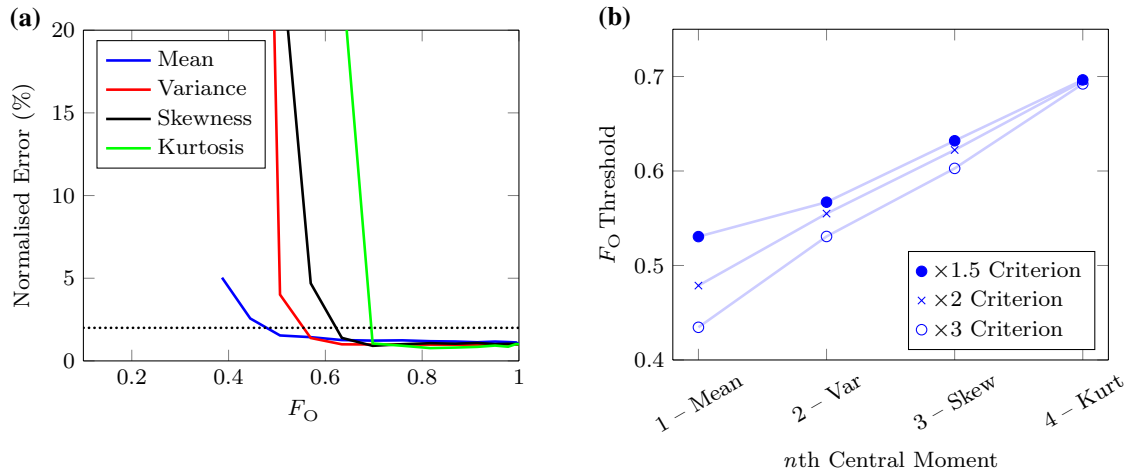

Fig. 8 **a** Averaged streamwise flow statistic errors (normalised) from all simulation cases. The dotted horizontal line at 2% normalised error illustrates the ×2 error criterion, one of three criteria applied to find the F_O thresholds shown in Fig. 8b. **b** F_O thresholds corresponding to each *n*th central moment of the averaged streamwise flow statistics

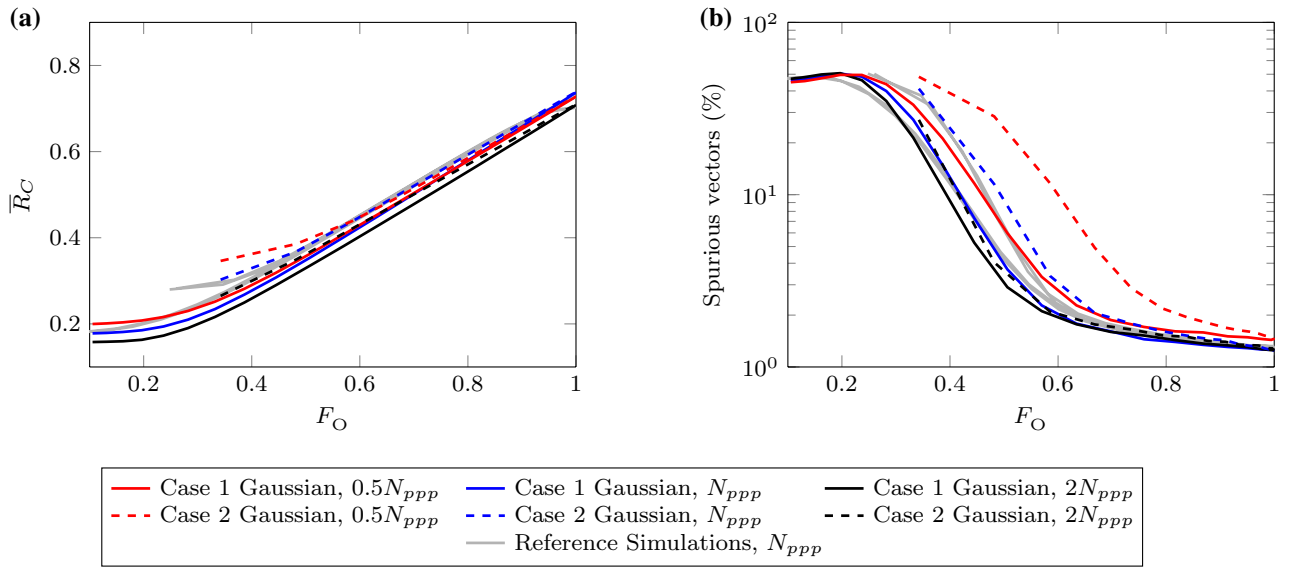

Fig. 9 Effect of different seeding densities, N_{ppp}, on **a** average correlation coefficient and **b** the proportion of spurious vectors. Different N_{ppp} are compared using case 1 and 2 Gaussian simulations, where case 1 shift mismatch results are shown using solid lines, while case 2 width mismatch results are shown with dashed lines. Case 1 and 2 top hat and super-Gaussian simulations are shown by solid grey lines for reference

successive laser profiles (and thus a high F_O value). As would be expected, higher order flow statistics can display greater sensitivity to laser mismatch, with inferior robustness to low F_O values when compared with lower order statistics (mean flow, for example).

2.6 Impact of seeding density

Figure 9 shows the effect of different seeding densities (N_{ppp}) on the correlation coefficient and spurious vector proportion of case 1 and 2 Gaussian profile simulations. These simulations consider PIV images with seeding half

as dense ($0.5N_{ppp}$) and twice as dense ($2N_{ppp}$), as the simulations presented previously in Sect. 2.

Case 1 simulations display behaviours consistent with conventionally seeded results for both correlation coefficient and spurious vector detection, although higher seeding scenarios result in the detection of marginally fewer spurious vectors. In addition, it is important to note that case 1 shift mismatch simulations maintain constant seeding densities in simulation images, even under severe misalignment, since the width and shape of the light sheets remain unchanged. Case 2 width mismatch scenarios, however, consider one light sheet that becomes narrower than the other, which consequently reduces the seeding density in the PIV image corresponding to the narrower light sheet at lower F_O values. This explains why, in Fig. 4b of Sect. 2.4, case 2 spurious vectors deviate slightly from case 1 results at low F_O. When adding further reductions to seeding density ($0.5N_{ppp}$), greater deviation from spurious detection trends at low F_O is observed due to severe narrowing of one light sheet pulse. However, in these $0.5N_{ppp}$ cases, with even moderate width mismatch, the reduction in seeding density reaches extreme levels that would be considered unrealistic in any carefully conceived PIV measurement. Similar case 1 and 2 behaviours are also observed in the streamwise mean and turbulence intensity error (not shown), with deviations only found in case 2 simulations at low F_O. In summary, our results suggest that under typical PIV measurement conditions, changes to seeding density do not have any significant impact on the sensitivity to laser mismatch.

2.7 Other considerations

Image pre-processing techniques were also investigated for their impact on the sensitivity to laser mismatch, where min–max filtering (Westerweel 1993) and histogram equalisation (Adrian and Westerweel 2011) algorithms were considered. However, image pre-processing operates by normalising particle image intensities (determined by the algorithm input parameters), thereby increasing the uniformity of the image and making the effective light sheet intensity distribution more "top hat-like". In this process, the effective thickness of the light sheet contributing to correlation is also increased (along with any associated spatial attenuation over the light sheet-normal direction). By artificially altering the light sheet intensity distribution in this way, the actual light sheet intensities I_{01} and I_{02} used in the calculation of F_O (Eq. 3) are no longer representative of effective light sheet mismatch conditions, and Eq. 3 underestimates the effective F_O of the PIV image pair. Simulations verify this limitation, where image pre-processing applied to top hat profile scenarios (which has a limited impact on images, since the profile is already a uniform top hat) show consistent behaviours with prior results (not shown here for brevity). Meanwhile, the results from Gaussian profile scenarios with image pre-processing exhibit the same kind of degradation in correlation coefficient and increase to errors and spurious vectors, but these responses have been shifted to lower F_O values when calculated using Eq. 3. Appropriate correction of the F_O equation for use with image pre-processing, or the direct calculation of F_O from PIV images (Scharnowski and Kähler 2016; Scharnowski et al. 2017) should generalise behaviours in pre-processing scenarios, but is beyond the scope of this work. Image pre-processing, therefore, has the potential to increase robustness to laser mismatch after PIV images have been captured, but the effectiveness of these algorithms can depend on the uniformity of the actual laser profiles, as well as the extent of PIV image noise and artefacts. Appropriate tuning of a PIV experiment's laser mismatch prior to image capture will always result in superior measurements, since they involve a fundamentally higher quality data set that is less dependent on processing algorithm performance.

Some outlined light sheet mismatch scenarios can be readily identified using a variety of laser alignment techniques. However, undertaking a challenging PIV measurement configuration can demand increased care and precision in light sheet alignment and matching, which may require detailed, quantitative laser profiling to balance various experimental compromises. For example, highly spread light sheets are necessary in PIV measurements over large fields of view, where variations in each laser's beam profile can translate to changes in light sheet mismatch over the measurement domain. Any adjustments to the light sheet, to improve the light sheet overlap in the centre of the field of view, for example, must balance with the impacts on overlap elsewhere in the field of view. Similarly, multiple pulse PIV may require the alignment of multiple PIV laser systems, and depending on the correlation algorithm employed, this configuration may be more sensitive to laser mismatch (due to an additive mismatch effect). Refinement of light sheet profile mismatch can, therefore, be critically important to the quality of many PIV measurements.

3 Experimental laser misalignment

To complement and validate the simulation results outlined in Sect. 2.4, a PIV experiment has been performed involving the deliberate mismatch of the laser light sheet.

3.1 Experimental configuration

Two-pulse, 2D PIV measurements were taken of a Re_θ = 7500 (approx.) turbulent boundary layer in the High Reynolds Number Boundary Layer Wind Tunnel (HRNBLWT) at the University of Melbourne (for further details regarding this facility, see Nickels et al. 2005). Data were

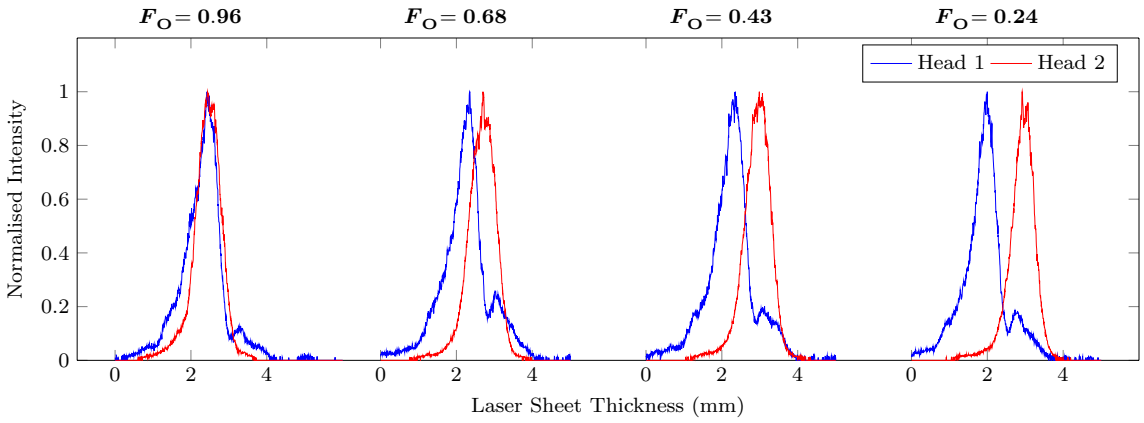

Fig. 10 Selection of tested laser sheet overlap profiles (with normalised intensity), from best overlap (left) to worst (right)

captured in the streamwise–spanwise plane over a region measuring 4200 × 6300 viscous units (or 175 mm × 265 mm, streamwise × spanwise), and at a wall-normal height of approximately 240 viscous units (∼ 10 mm). Additional details regarding the features of this experimental PIV configuration can be found in de Silva et al. (2015). PIV images were captured using a single 10.7 megapixel PCO 4000 PIV camera and a Nikon AF Micro-Nikkor 60 mm 2.8D lens, providing an image resolution of 2672 × 4008 pixels (streamwise × spanwise) and a flow resolution of approximately 1.6 viscous units/pixel. Note that the experimental field of view and spatial resolution in viscous units are effectively identical to that considered by the simulations, as outlined in Sect. 2 (with only negligible variations between the two cases). A Spectra-Physics Quanta-Ray PIV-400 pulsed 532 nm Nd:YAG laser (nominally at 400 mJ/pulse) was used over a 10 m beam path to generate the laser light sheet. The resulting light sheet intensity profiles were captured using a low-cost laser profiling device, which is detailed in the Appendix.

The beam combining optics of the laser are readily accessible in the front of the laser unit used in this experiment. Therefore, measurements were taken by misaligning the laser beam using the combining optics, and then allowing the laser to stabilise (to ensure the laser is at thermal equilibrium—for further discussion of the thermal equilibrium impacts on PIV laser operations, see Grayson et al. 2017). While operating the wind tunnel at a reduced speed for safety reasons, multiple laser profiles of the light sheet (to average laser jitter effects) were captured at the centre of the experimental field of view. The wind tunnel was then returned to the measurement velocity and allowed to stabilise, before capturing a set of 120 PIV image pairs. This process was repeated for eight distinct laser alignment and mismatch combinations. Figure 10 shows a selection of the resulting laser profiles, along with their corresponding F_O values.

Seeding in this measurement was provided by polyamide particles and image pairs were captured with a time interval of $\Delta t = 110$ µs, corresponding to a mean pixel displacement of ∼ 11 pixels. The same multipass correlation algorithm with window deformation used in Sect. 2 was applied to process these experimental images, with initial interrogation windows of 64 × 64 pixels, and a final window size of 32 × 32 pixels.

3.2 Experimental results

The average correlation coefficient for the experimental data set is plotted with black triangle (△) symbols, as shown in Fig. 11a. While the simulations in Sect. 2 (also shown in Fig. 11a with the grey lines) isolate light sheet mismatches of profile width or alignment in distinct scenarios, experimental light sheet profiles involve combinations of alignment, width, and shape mismatches (clearly observed in Fig. 10). Therefore, the experimental data presented here combine shift and width mismatches, as well as incorporating unsimulated mismatches in the shape of each light sheet intensity profile (which are beyond the scope of this study). Despite these complex interactions in the experimental results, the gradient at which the correlation coefficient degrades is consistent with earlier idealised simulation results, as presented in Sect. 2. The small offset observed between the correlation coefficient of the experiment and idealised simulation results is due to systematic differences in the image and correlation noise of these data sets. To confirm the cause of this offset, simulations rigorously matched to the experimental laser sheet profile and noise conditions were also performed, and are discussed in Sect. 3.3.

The proportion of spurious vectors resulting from these experiments are also compared with simulations in Fig. 11b, using common normalised median test parameters. While some scatter can be observed in the experimental results, many additional experimental errors can cause or influence

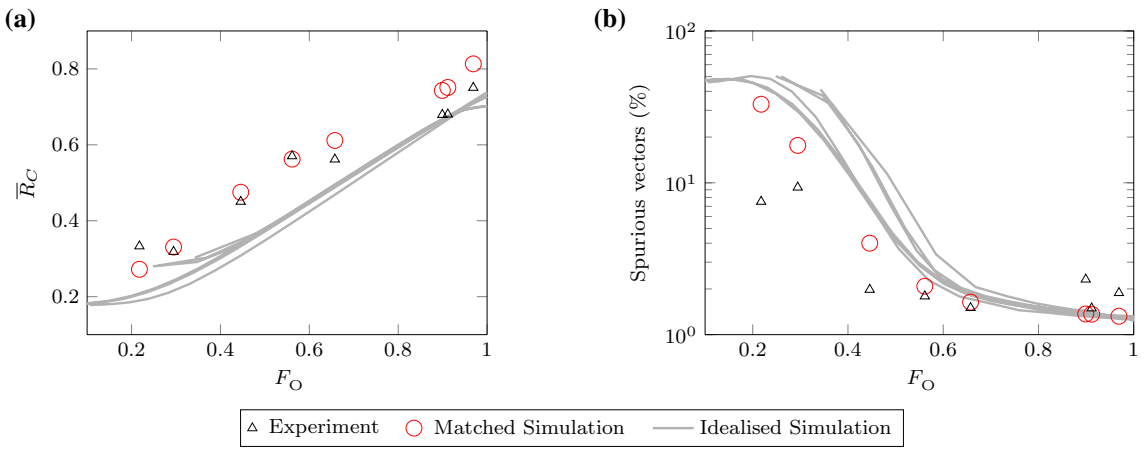

Fig. 11 Experiment and simulation results of laser profile mismatch on **a** average correlation coefficient and **b** proportion of spurious vectors

the spurious vectors detected in a PIV measurement. Nevertheless, a similar baseline proportion of spurious vectors under 'ideal' ($F_O \sim 1$) overlap conditions can be observed in experiment and simulation results. Furthermore, a rapid increase in experimental spurious vectors can be observed at an approximately similar F_O to that predicted by the simulations.

Due to the methodology of this experiment, the wind tunnel speed was reduced between the capture of each PIV image set to profile the laser light sheet. Consequently, small variations in wind tunnel speed were introduced between each measurement, making the direct comparison of experimental and simulation mean statistics difficult. However, a comparison of the streamwise turbulence intensity (shown in Fig. 12), normalised by the turbulence intensity under 'ideal' overlap conditions, shows reasonably good agreement in behaviour, with data exhibiting similar F_O thresholds beyond which the turbulence intensity rapidly increases.

3.3 Experiment-matched simulations

The simulation results from Sect. 2 can be further validated by running revised synthetic PIV simulations matched to the noise conditions observed in the experiment. While this matching is not necessary to compare the overall behaviour of the experimental results to simulations, it can verify the sensitivity of quantities to noise levels (e.g., the correlation coefficient). To this end, the experimental light sheet intensity profile from each laser head is captured with the laser profiling camera at the centre of the measurement field of view (as shown in Fig. 10), and rescaled for application to the simulation's illumination model. Dark field images from the PIV camera are also acquired to determine the background noise characteristics of the camera sensor, which defines the Gaussian noise distribution parameters applied to the simulation. Several additional simulation parameters are then iteratively tuned via comparative image measures to achieve close matching to an individual experimental PIV measurement.

The first comparative metric examines the average seeding particle diameter by autocorrelating interrogation windows over each of the experimental and simulation images, and averaging the results (outlined in Adrian and Westerweel 2011). This measure helps to match the simulation's particle diameter, and also the range and distribution of variations to particle diameter, by first considering the sharpest region of the experimental images (normally the centre of the image). Subsequently processing the entire image can account for particle diameter changes due to localised image focus variation and loss of sharpness at the corners of the PIV images, which can then be approximated by the simulation. Using this procedure, a cross-sectional comparison of a resulting experiment-matched autocorrelation peak is shown in Fig. 13a, averaged over the entirety of each image.

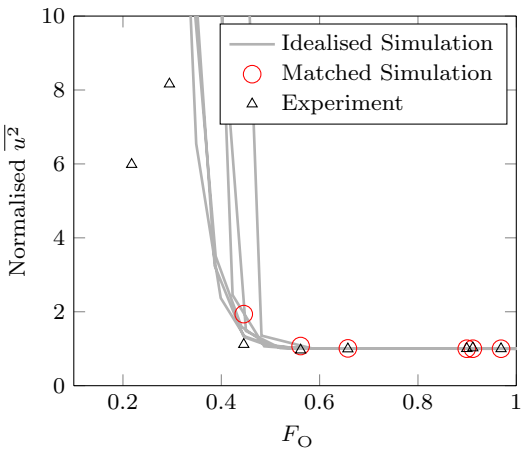

Fig. 12 Experiment and simulation results for normalised streamwise turbulence intensity ($\overline{u^2}$)

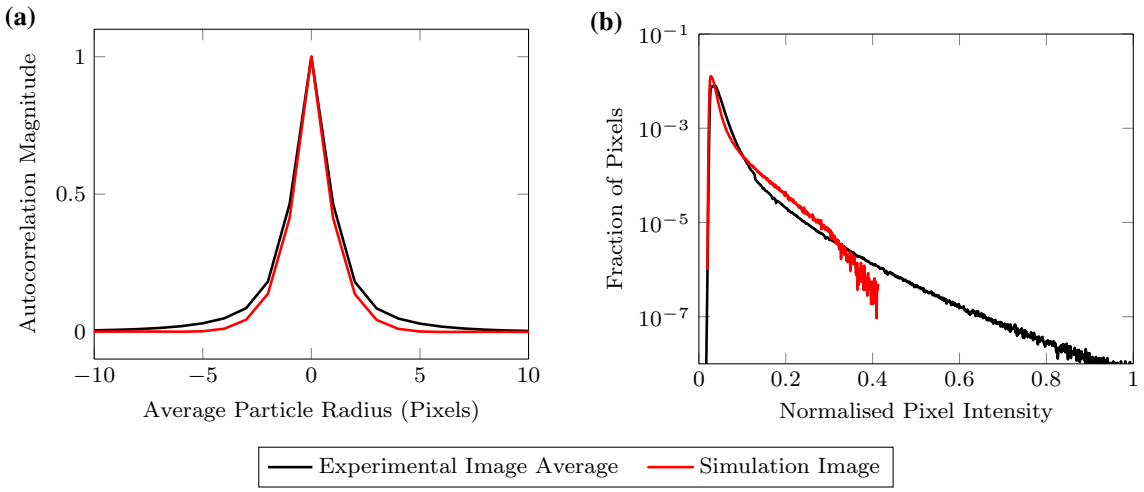

Fig. 13 **a** Average particle radius comparison of sample experimental and experiment-matched simulation distributions. **b** Normalised pixel intensity comparison of sample experimental and experiment-matched simulation histograms

The second comparison investigates the distribution of pixel intensities throughout each image (first used by Westerweel 2000). This plot allows tuning of the maximum simulation particle intensity, background noise and particle density, as well as further refinement of the loss of sharpness characteristics at the image edges. Figure 13b shows a sample comparison between pixel intensity distributions from an experiment and experiment-matched simulation.

Experiment-matched simulations, defined using this procedure, are tuned using experimental data and are compared with the PIV measurements in Figs. 11 and 12 (the matched simulations are indicated by the red circles, ○). Due to minimal changes in the configuration of the experimental setup, changes to the input light sheet profiles were the only necessary modification to simulation parameters across the tested scenarios—all other simulation parameters remained unchanged. Therefore, all variations to the correlation coefficient, spurious vector proportion, and streamwise turbulence intensity of the experiment-matched simulations are a direct result of different laser sheet profile alignment, mismatch and shape.

The comparison between the correlation coefficient of the experiment and matched simulations in Fig. 11a show good agreement, with only a slight scatter observed in the experimental results—likely to be caused by small variations in other experimental conditions and errors. Reasonably similar behaviour is also observed in comparisons of the spurious vector proportion (Fig. 11b) and streamwise turbulence intensity (Fig. 12). What is perhaps more revealing however, is that despite the extensive matching of simulation noise parameters and complex light sheet profiles to the experiment, the matched simulations show very similar behaviour to the idealised simulations presented in Sect. 2 (correlation coefficient offset excepted, due to fundamental differences in noise). Therefore F_O and these trends in measurement quality are relatively robust to a variety of complex and interacting laser mismatch conditions, including combinations of laser shift, width and shape mismatches. This matched comparison, therefore, validates the simulations presented in Sect. 2, confirming their robustness to experimentally realistic conditions and variations. They demonstrate that changes in light sheet alignment and profile width can have significant impacts on PIV image correlation and experimental results.

4 Conclusions

The impacts of laser light sheet misalignment and width mismatch have been systematically investigated in this study via a set of synthetic PIV image simulations and laboratory experiments. Results consistently reveal the rapid degradation in correlation quality which can occur when the two laser profiles used to capture a PIV image pair are no longer well matched, either in the width or alignment of their intensity profiles. In particular, the quantities and flow statistics of interest in an experiment can dictate the sensitivity of light sheet mismatch on experimental errors. However, the analysis from this study indicates that an $F_O > 0.8$ setup should avoid the severe measurement errors associated with laser overlap. Provided $F_O > 0.8$, we observe a negligible impact on the measurement of up to fourth-order flow statistics while also providing an operational margin for robustness to dynamic, shot-to-shot laser instabilities.

A PIV experiment involving various light sheet alignment and mismatch scenarios is outlined, and coupled with experiment-matched PIV simulations, these data confirm the

significance of good laser overlap and the robustness of the simulation results. The overlap and matched intensity profile of PIV laser light sheets proves to be critical for the capture of quality data. However, laser analysis tools such as a laser profiling camera can offer a clear, user friendly path towards improved PIV measurements.

Acknowledgements The authors wish to thank the Australian Research Council and the Australian Government Research Training Program Scholarship for their financial support of this research.

Appendix

A low-cost laser profiling camera using readily available off-the-shelf components is used in this study to capture laser behaviours. This appendix outlines the components of the camera design and the procedure for its use in PIV measurements.

Camera configuration

The laser profiling system uses a mirrorless interchangeable lens camera with a large APS-C size sensor measuring 22.3×14.9 mm^2, able to comfortably fit the unfocused laser beams used in typical PIV experiments. A Canon EOS-M camera body is used for this purpose (no lens is required), containing an 18 megapixel sensor that results in a pixel density of ~230 px/mm (see ⑤ in Fig. 14a). We note that more conventional digital single-lens reflex (SLR) cameras have also been tested with success. A wired remote trigger is used with a Wi-Fi enabled SD card to remotely capture and review images in near real-time (some cameras may also allow USB tethered image capture). An overview of this setup is shown in Fig. 14b.

Due to the sensitive electronics found in digital cameras, attenuation optics are needed to image a laser profile without damaging the camera sensor. These optics also require the flexibility to adjust filter strength to tune image exposure for different setups and laser powers. In this study, as with prior published works (Cignoli et al. 2004; Langer et al. 2013), neutral density filters are used to achieve the necessary attenuation. These optics are commonly available with threaded mounts and in a variety of strengths to be stacked, mixed, and matched. The laser profiling setup uses a combination of laser-grade neutral density filters and standard photographic neutral density filters used for still photography. Laser-grade neutral density filters are ideal for this application, purpose built to take the energy densities found in laser profiling. Photographic neutral density filters, however, have the advantage of being inexpensive and readily available in a variety of filter strengths. They are also capable of withstanding a surprising amount of laser energy, although it should be noted that a gradual change in filter characteristics has been observed over long term use. The profiling setup in this study uses a variety of photographic neutral density filters of different strengths (③ in Fig. 14a), and a laser-grade neutral density filter is added to the top of the filter stack via a threaded adapter (① and ② in Fig. 14a) when profiling higher energy laser beams (such as 400 mJ/pulse 532 nm beams).

These filters thread onto a metal filter step ring that is epoxied to a 3D printed camera lens mount (④ in Fig. 14a). This mount locks into the camera as required and angles the filters off the sensor plane to prevent any laser reflections returning through the beam path into the laser unit and causing damage. The solid green line in Fig. 14a shows the incident path of a sampled laser beam and the dotted green line indicates the direction of any surface reflections off the neutral density filters.

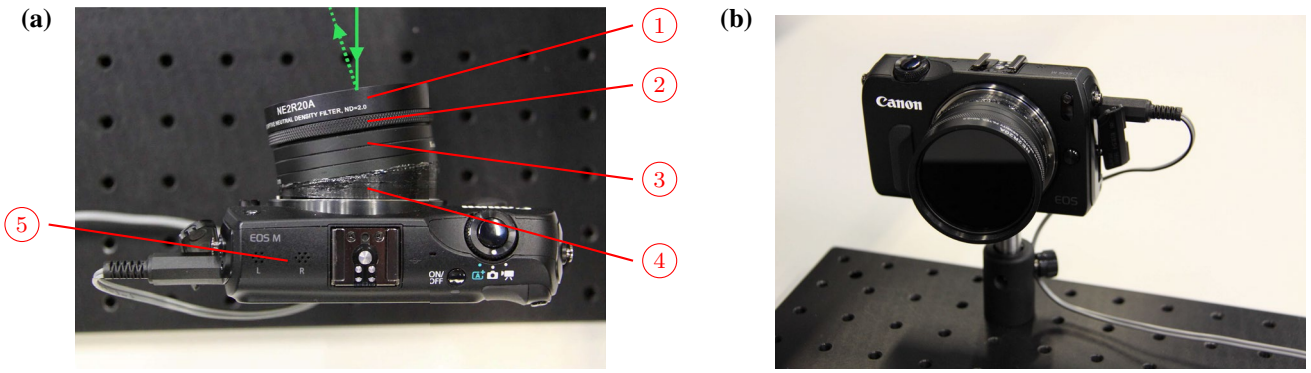

Fig. 14 Laser profiling camera setup **a** annotated top view and **b** perspective view. Annotations in **a** denote ① the laser-grade neutral density filter, ② laser-grade filter threaded adapter, ③ photographic neutral density filters, ④ 3D printed camera lens mount with epoxied metal filter thread, ⑤ interchangeable lens camera body

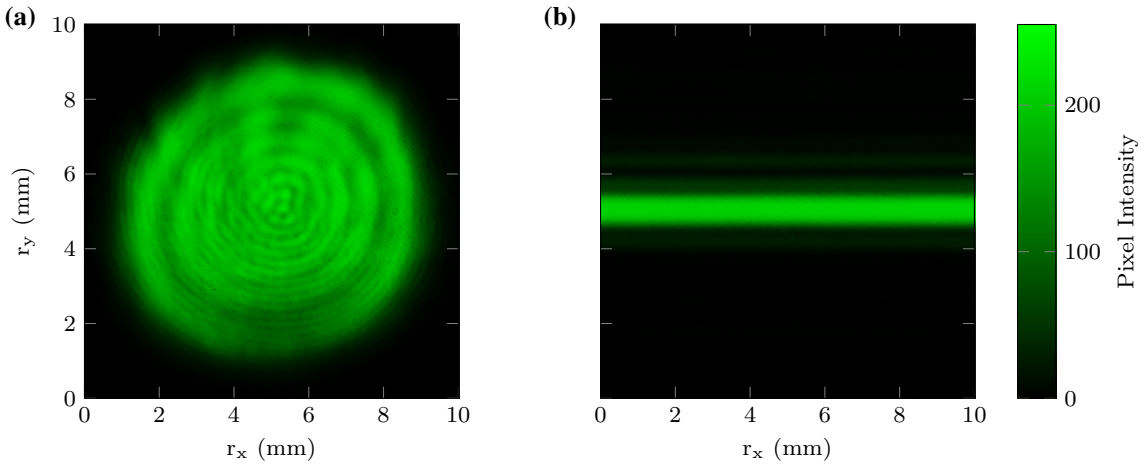

Fig. 15 **a** Imaged laser beam profile and **b** a captured laser light sheet profile. r_x and r_y denote the horizontal and vertical image dimensions in physical space

Since this camera contains an RGB colour imaging sensor (using a Bayer filter array), only the most relevant interpolated colour channel is considered in analysis; for example, the green channel is isolated when imaging 532 nm lasers. Laser profile features of significance are typically on the order of 0.1–1 mm, much larger than the 0.0043 mm pixel size of the imaging sensor. Therefore, Bayer filter interpolation effects are considered to have a negligible impact on results and spatially interpolated RAW camera images are captured for laser profile analysis. Consumer cameras also incorporate a non-linear pixel brightness behaviour (defined by the gamma correction factor, γ) into processed images by default, to mimic the non-linear interpretation of brightness by the human eye. RAW images must, therefore, be processed with a gamma correction, where $\gamma = 1$, to ensure a linear brightness response. To achieve this, the DCRaw software package (Coffin 2008) is used to process the RAW camera images and ensure that the resulting TIFF image files contain the corrected linear brightness response for quantitative analysis.

Figure 15a shows a sample laser beam profile captured with the device. We note that the pattern of concentric rings is due to thermal lensing within the cavity and is considered typical of this particular Nd:YAG laser. However, a slight asymmetry of the beam can also be identified in this image which would have been difficult to observe in many burn tests, where the top of the profile is slightly brighter than the bottom. Although these asymmetries are often overlooked, they can have significant consequences when the beam is spread into a laser sheet for PIV, causing asymmetric or multi-lobed laser sheet profiles. These irregular profiles can make profile matching of the two PIV laser beams more difficult. Figure 15b shows a laser sheet profile from a similar 532 nm Nd:YAG laser.

Camera applications

This laser profiling camera has numerous potential applications for laser tuning, diagnostics, and experimental setup. Profiling a laser beam can reveal non-uniformities in the beam profile, overlap issues and potential faults in the laser unit. Regular measurements of beam profiles can also monitor incremental degradation of laser performance and inform service schedules for laser equipment. Dynamic laser behaviours such as the time required for the laser to warm up and reach thermal equilibrium from a cold start, or shot-to-shot beam stability have been recognised as important factors when performing PIV experiments (Kähler and Kompenhans 2000; Fond et al. 2015; Grayson et al. 2017). A camera-based laser profiler, such as the device discussed in this study, is capable of quantifying and monitoring these behaviours in a given laser unit.

Laser light sheets can also be profiled with this device (see Fig. 15b), and these measurements can be crucial to ensuring well-matched laser sheet profiles for PIV images. The alignment and intensity distributions of the light sheet can be quantified across the measurement region to optimise PIV image quality over the entire field of view.

Furthermore, this laser profiling system is not restricted to use with PIV equipment, and can be used in a large range of experiments involving laser devices. Tests with this setup have also been performed on a Laser Doppler Anemometry system to verify laser crossover locations and symmetry, beam stability, and profiles. To date, this device has captured data from 120 mJ/pulse up to 400 mJ/pulse Nd:YAG 532 nm pulsed PIV lasers, as well as continuous 12 W 485–529 nm Argon Ion, ~ 90 mW 660 nm red diode and 785 nm infrared diode laser beams.

References

Adrian RJ, Westerweel J (2011) Particle image velocimetry. Cambridge University Press, Cambridge

Andrèbe Y, Behn R, Duval BP, Etienne P, Pitzschke A (2011) Use of webcams as tools for alignment and supervision of a Thomson scattering system in the near infrared. Fusion Eng Des 86(6):1273–1276

Blinde PL, Lynch KP, Schrijer FFJ, Van Oudheusden BW (2015) Determination of instantaneous pressure in a transonic base flow using four-pulse tomographic PIV. In: 11th International Symposium on Particle Image Velocimetry

Brücker C, Hess D, Kitzhofer J (2012) Single-view volumetric PIV via high-resolution scanning, isotropic voxel restructuring and 3D least-squares matching (3D-LSM). Meas Sci Technol 24(2):024001

Cignoli F, De Iuliis S, Zizak G (2004) A webcam as a light probe beam profiler. Appl Spectrosc 58(11):1372–1375

Coffin D (2008) DCRAW: Decoding raw digital photos in Linux

de Silva CM, Baidya R, Khashehchi M, Marusic I (2012) Assessment of tomographic PIV in wall-bounded turbulence using direct numerical simulation data. Exp Fluids 52(2):425–440

de Silva CM, Squire DT, Hutchins N, Marusic I (2015) Towards capturing large scale coherent structures in boundary layers using particle image velocimetry. In: 7th Australian Conference on Laser Diagnostics in Fluid Mechanics and Combustion

Elsinga GE, Van Oudheusden BW, Scarano F (2006) Experimental assessment of tomographic-PIV accuracy. In: 13th International Symposium on Applications of Laser Techniques to Fluid Mechanics

Fond B, Abram C, Beyrau F (2015) On the characterisation of tracer particles for thermographic particle image velocimetry. Appl Phys B 118(3):393–399

Ganapathisubramani B, Longmire EK, Marusic I, Pothos S (2005) Dual-plane PIV technique to determine the complete velocity gradient tensor in a turbulent boundary layer. Exp Fluids 39(2):222–231

Grayson K, de Silva CM, Hutchins N, Marusic I (2017) Beam stability and warm-up effects of Nd:YAG lasers used in particle image velocimetry. Meas Sci Technol 28(6):065301

Kähler CJ, Kompenhans J (2000) Fundamentals of multiple plane stereo particle image velocimetry. Exp Fluids 29(1):S070–S077

Keane RD, Adrian RJ (1992) Theory of cross-correlation analysis of PIV images. Appl Sci Res 49(3):191–215

Langer G, Hochreiner A, Burgholzer P, Berer T (2013) A webcam in Bayer-mode as a light beam profiler for the near infra-red. Optics Lasers Eng 51(5):571–575

Lewis JP (1995) Fast normalized cross-correlation. Vis Interface 10:120–123

Mistry D, Dawson J (2014) Experimental investigation of multiscale entrainment processes of a turbulent jet. In: 17th International Symposium on Applications of Laser Techniques to Fluid Mechanics

Mullin JA, Dahm WJA (2005) Dual-plane stereo particle image velocimetry (DSPIV) for measuring velocity gradient fields at intermediate and small scales of turbulent flows. Exp Fluids 38(2):185–196

Naka Y, Tomita K, Shimura M, Fukushima N, Tanahashi M, Miyauchi T (2016) Quad-plane stereoscopic PIV for fine-scale structure measurements in turbulence. Exp Fluids 57(5):1–20

Nickels TB, Marusic I, Hafez S, Chong MS (2005) Evidence of the -1-law in a high-Reynolds-number turbulent boundary layer. Phys Rev Lett 95(7):074501

Nobach H (2011) Influence of individual variations of particle image intensities on high-resolution PIV. Exp Fluids 50(4):919–927

Nobach H, Bodenschatz E (2009) Limitations of accuracy in PIV due to individual variations of particle image intensities. Exp Fluids 47(1):27–38

Pfadler S, Dinkelacker F, Beyrau F, Leipertz A (2009) High resolution dual-plane stereo-PIV for validation of subgrid scale models in large-eddy simulations of turbulent premixed flames. Combust Flame 156(8):1552–1564

Scarano F, Elsinga GE, Bocci E, van Oudheusden BW (2006) Investigation of 3-D coherent structures in the turbulent cylinder wake using tomo-PIV. In: 13th International Symposium on Applications of Laser Techniques to Fluid Mechanics

Scharnowski S, Kähler CJ (2016) Estimation and optimization of loss-of-pair uncertainties based on PIV correlation functions. Exp Fluids 57(2):1–11

Scharnowski S, Grayson K, de Silva CM, Hutchins N, Marusic I, Kähler CJ (2017) Generalization of the PIV loss-of-correlation formula introduced by Keane and Adrian. Exp Fluids 58(10):150

Sillero JA, Jiménez J, Moser RD (2013) One-point statistics for turbulent wall-bounded flows at Reynolds numbers up to $\delta+$ 2000. Phys Fluids 25(10):105102

Westerweel J (1993) Digital particle image velocimetry. PhD thesis, Delft University

Westerweel J (2000) Theoretical analysis of the measurement precision in particle image velocimetry. Exp Fluids 29(1):S003–S012

Westerweel J, Scarano F (2005) Universal outlier detection for PIV data. Exp Fluids 39(6):1096–1100

Wieneke B (2005) Stereo-PIV using self-calibration on particle images. Exp Fluids 39(2):267–280

Worth NA, Nickels TB, Swaminathan N (2010) A tomographic PIV resolution study based on homogeneous isotropic turbulence DNS data. Exp Fluids 49(3):637–656